RSC Advances

PAPER

View Article Online
View Journal | View Issue

Check for updates

Cite this: *RSC Adv.*, 2022, **12**, 11391

Revealing the structural and chemical properties of copper-based nanoparticles released from copper treated wood

Chen Wang *[a] and Chaolong Qi [b]

Copper-based preservatives consisting of micronized and nanoscale copper particles have been widely used in applications for wood protection. The widespread use of these preservatives along with the potential release of copper-containing nanoparticles (Cu NPs) during the life cycle of treated wood, has raised concerns over the impacts on the environment and occupational exposure. Along with assessing the potential hazards of these materials, a critical step is determining the chemical and morphological characteristics of the copper species released from copper-treated wood. Therefore, a combination of scanning transmission electron microscopy (STEM) and electron energy-loss spectroscopy (EELS) was utilized to characterize and differentiate the released copper-containing particles based on their structures, sizing, and chemical properties. Airborne wood dust samples were collected during the abrasion and sawing of micronized copper (MC) treated wood in a laboratory testing system. Based on the signature Cu $L_{2,3}$ edge of EEL spectra, three different copper species (*i.e.*, basic copper carbonate, copper, and copper–wood complex) were identified as major components of the embedded particles in wood dust. In addition, two types of individual Cu NPs consisting of basic copper carbonate and copper were identified. The variation of morphologies and chemical properties of copper-containing particles indicates the importance of copper–wood interactions to determine the formation and distribution of copper species in wood components. Our findings will advance the fundamental understanding of their released forms, potential transformation, and environmental fate during the life cycle.

Received 22nd February 2022
Accepted 6th April 2022

DOI: 10.1039/d2ra01196d

rsc.li/rsc-advances

Open Access Article. Published on 11 April 2022. Downloaded on 1/12/2026 6:28:32 AM.
This article is licensed under a Creative Commons Attribution-NonCommercial 3.0 Unported Licence.

Introduction

A variety of wood preservatives have been used in pressure-treated lumber (PTL) to extend the useful service life and enhance the performance of wood products. In many wood preservative formulations, copper-based ingredients are frequently used as the main biocides to protect wood structures against fungal, microbial, and insect decay.[1] Recently, new particulate copper (*i.e.*, micronized copper or MC) compounds were introduced to the wood preservation industry to replace the conventional ionized copper preservatives used in pressure-treated wood.[2,3] Most MC preservatives consist of basic copper carbonate (BCC) particles and an organic co-biocide dispersed in water.[4] Other copper-based chemicals such as copper hydroxide, copper oxychloride, copper sulfate, cuprous oxide, copper hydroxycarbonate, or other copper organic compounds may also be used as active ingredients in the formulation of copper-based treatment.[5] MC preservatives are made by wet milling an aqueous dispersion containing particulate copper compounds.[3] The resulting aqueous slurry contains "micronized" copper particles defined by their sizes ranging from 1 nm to 25 μm.[3] After pressure treatment, large particles from the preservatives tend to retain their native chemical states and accumulate on the wood cell walls.[3,6] However, the smaller copper-containing particles that penetrate the cell membranes are likely to interact with other cellular elements of the wood, leading to substantial changes in particle morphologies and chemical properties. As a result, airborne dust generated during the mechanical processing of copper-treated wood may contain multiple Cu species with various physicochemical properties. Understanding the properties of emitted particles will improve the assessment of these materials' exposure hazards, potential health effects, and environmental impacts.

Similar to other metal oxide nanoparticles, a size-dependent effect was observed from several studies evaluating the toxicity of micro- and nano-sized copper oxide (CuO) particles.[7,8] *In vitro* studies have suggested that exposure to CuO NPs may lead to intense oxidative stress and inflammation in lung tissues.[9] Size-dependent toxic effects are primarily ascribed to the higher surface reactivity and greater surface area of the nanoscale particles than those of micro-sized counterparts. Besides particle sizes, the toxicity of the released Cu NPs is also influenced by their chemical forms and the exposed environment.

[a]*The Health Effects Lab Division, National Institute for Occupational Safety and Health, Cincinnati, OH, 45226, USA. E-mail: xli7@cdc.gov*
[b]*Division of Field Studies and Engineering, National Institute for Occupational Safety and Health, Cincinnati, OH, 45226, USA*

© 2022 The Author(s). Published by the Royal Society of Chemistry

Open Access Article. Published on 11 April 2022. Downloaded on 1/12/2026 6:28:32 AM. This article is licensed under a Creative Commons Attribution-NonCommercial 3.0 Unported Licence.

During the pressure treatment process, an abundance of aqueous preservatives containing ionic copper compounds can infuse through the cellular structures of wood components. These mobile copper species can react with the phenol and carboxyl functional groups from hemicelluloses, pectins, or lignins in wood components, forming various copper–wood complexes.[5,10] Depending on the chemistry of absorption sites in the wood structure, precipitation may occur and form copper, copper carbonates, copper oxides, and organic copper compounds.[5] The environmental changes can also contribute to the chemical transformation of these compounds by oxidation, dissolution, and sulfidation and hence affect the forms of copper species that are released into the environment.[11]

Studies of the chemical transformation of copper-based nanomaterials have indicated that complex chemical reactions of copper species can occur in many biological systems and natural environments.[10–13] During the treatment with micronized copper preservatives, most insoluble copper particles (as a form of BCC) are immobilized in the polymeric matrices of wood structures. In contrast, the soluble copper species (*i.e.*, mobile Cu(II) ions) actively react with wood cell acidic sites. These rapid reactions happen in many wood cellular components consisting of carboxylic acid, aromatic esters, and phenolic hydroxyl groups, forming stable copper–wood complexes bound to the wood matrices.[10,12,13] Therefore, the dust collected from sawing or abrasion of the treated wood may contain different levels of reacted Cu(II) complex and/or unreacted BCC particles with distinctive physicochemical properties. Identifying and characterizing these copper species based on their morphologies, sizes, and chemical states would be vital before evaluating their potential hazards after being released into the environment.

It is noted that pressure treatment cannot guarantee a homogeneous penetration of copper preservatives into wood structures. The penetration depth and distribution of copper species in wood are affected by the formulation of the preservatives, the sizes of copper particles, the types of wood species, and the chemistry of copper–wood interaction. Accordingly, researchers have employed various analytical techniques to understand the micro-distribution, mobility, and chemical transformations of Cu NPs in copper-treated wood. The distribution and deposition characteristics of Cu NPs in wood structures were first studied by scanning electron microscopy (SEM) combined with energy-dispersive X-ray spectroscopy (EDS).[6] Matsunaga *et al.*[6] showed that insoluble copper carbonate particles (rectangular shape in sizes ranging from 50 to 700 nm) tend to agglomerate on or around pits that connect cellular elements in wood and on cell walls. They also detected a low level of copper element in the cell walls of latewood fibers, resulting from the penetration of nanoscale Cu particles into the nanocapillary network and interfiber transport within the wood cell components. Most recently, synchrotron-based X-ray fluorescence microscopy (XFM)[14] and X-ray Micro Computed Tomography (X-ray Micro-CT)[15] were used to investigate the spatial distribution of copper content to estimate the penetration depth of copper in wood structures. Unlike insoluble copper precipitates, mobile ionic copper can infiltrate wood cell walls and chemically bind to specific cellular components by fixation reactions. Additionally, researchers have employed multiple spectroscopic techniques such as electron paramagnetic resonance (EPR) spectroscopy[10,12,13] and X-ray absorption near-edge spectroscopy (XANES)[14,16] to quantify the reacted copper species and identify their oxidation states in treated wood. Although copper species can be characterized using EPR and XANES for bulk materials, the localization of copper in specific wood structures and their corresponding chemical states remain unclear. As an essential tool for nanoscale imaging, transmission electron microscopy (TEM) has been combined with analytical spectroscopy techniques to study wood ultrastructures and chemical components.[17,18] However, the applications of the conventional TEM techniques for chemical speciation in wood samples are still limited because of the potential radiation damage of wood samples induced by the high dose electron beam and the detector's low sensitivity to the light elements. An alternative technique to mitigate the beam damage issues is to use Z-contrast imaging offered by the Scanning Transmission Electron Microscope (STEM). Once performed in conjunction with electron energy loss spectroscopy (EELS), this method can provide rich information on materials' local composition, chemistry, and structure in unprecedented resolution.[19]

In this work, we proposed a new approach for sampling and characterizing airborne Cu NPs released during the mechanical abrasion and sawing of copper-treated wood. The objectives of this study include: (a) determine morphologies and micro-distribution of copper species in wood dust particles generated during the mechanical processing (*e.g.*, sanding or sawing) of copper-treated wood; (b) compare different forms of Cu NPs (unbonded or embedded in wood matrices) present in the airborne wood dust samples; (c) identify the elemental composition and chemical states of released Cu NPs and evaluate factors that may contribute to the formation and release of copper during handling and use of copper-treated wood.

Materials and methods

Materials

Two types of commercial lumber were purchased from local hardware stores for this study: untreated yellow pine (UYP) and lumber treated with micronized copper azole (MCA) preservatives. The copper-treated lumber had retention levels rated for ground contact applications. Specifically, MCA lumber was rated at a retention level of 0.14 pounds of chemicals per cubic foot (PCF, equivalent to 2.2 kg m^{-3}) with dispersed copper carbonate and tebuconazole as active ingredients. Reference materials including Cu(II) acetate ($Cu(OAc)_2$, powder, 99.99%), Cu(I) oxide (Cu_2O, powder, 97%), Cu(II) oxide (CuO, nanopowder, average particle size < 50 nm), basic copper carbonate ($CuCO_3 \cdot Cu(OH)_2$, powder, reagent grade) and Cu (nanopowder, average particle size = 25 nm) were purchased from Sigma Aldrich (St. Louis, MO) for EELS measurements. These materials were used as analogs for Cu compounds that might be present in the airborne dust samples.

© 2022 The Author(s). Published by the Royal Society of Chemistry

Open Access Article. Published on 11 April 2022. Downloaded on 1/12/2026 6:28:32 AM.
This article is licensed under a Creative Commons Attribution-NonCommercial 3.0 Unported Licence.

Thin section samples

Thin section samples were prepared by cutting the wood strips cross-sectional and longitudinal using a sliding microtome (Part No. 162-3012, Uchida Yoko, Japan). Then, the uncoated sections were attached to aluminum stubs using double-sided carbon tape to be analyzed by an SEM.

Aerosol samples

An automatic laboratory tool-testing system (Fig. 1) was used to generate wood dust aerosols during sawing and sanding wood samples. A dust collection and air handling unit (PSKB-1440, ProVent LLC, Harbor Springs, MI) was used as an air mover for the system. The air handling unit was set to draw pre-filtered room air into the testing system at a flow rate of 0.64 m^3 s^{-1} (equivalent to 1350 cubic feet per minute (CFM)). During a sawing test, the system was programmed to run a circular saw (model CS10, Robert Bosch Tool Corp., Mt. Prospect, IL) with a thin-kerf finishing blade having 36 carbide teeth (model DW3176, DeWalt Industrial Tool Co., Towson, MD) and make a preset number of repeated crosscuts at a cutting feed rate of 2.54 cm s^{-1}. A brand new saw blade was used for each type of lumber, and the system was thoroughly cleaned between tests of different lumber types to prevent cross-contamination. For the sanding test, a variable-speed belt sander (model 352VS, Porter-Cable, Jackson, TN) was used to sand the surface of a lumber board as the board was advanced along its length using the automatic feeding mechanism. The sander used 240-grit sanding belts (Metalite R228 Abrasive Belt, Aluminum Oxide, Cotton Backing, Norton Saint-Gobain Abrasives, Worcester, MA). Two to three brand new belts were used in each sanding test to ensure proper particle loading on collected samples. A dust cloud generated by each sawing or sanding path was carried downstream by the airflow through the tool-testing chamber and duct before being sampled by the sampling device. The detailed testing procedures and the diagram of the laboratory testing system can be found in recent studies.[20–22] In addition, baseline tests were performed when the saw/sander was running but not sawing/sanding any wood to measure the emission from the machines.

The dust samples were collected on 37 mm diameter, 0.45 μm pore-size Mixed Cellulose Esters (MCE) membrane filters (Part Number 225-9, SKC Inc., Eighty Four, PA) supported by backup pads (Part Number 225-27, SKC Inc., Eighty Four, PA) in three-piece electrically-conductive filter cassettes (Part Number 225-309, SKC Inc., Eighty Four, PA) by following the modified NIOSH Method 7402.[23,24] The sampling flow rate was 12.5 L min^{-1}. A cyclone pre-separator with a D_{50} of 0.9 μm at this flow rate was used to take these samples through one of the two sampling probes, as shown in Fig. 1. The loss for the targeted particles (D_{50} of 0.9 μm) in the sampling line was negligible based on calculations.[25] Three filter samples and one field blank for each lumber type were collected during the sanding/sawing of treated lumber. Sampling volume was varied to determine the optimum loading of filters for TEM analysis. The MCE filters with the optimum loading were processed and transferred to 200-mesh nickel TEM grids (Part Number 2620N-XA, Structure Probe Inc., West Chester, PA) using the modified NIOSH Method 7402 for airborne carbon nanotubes and nanofibers.[26,27]

Analytical methods

The wood sample thin sections were examined by using a Phenom XL SEM (Thermo Fisher, Hillsboro, OR) in the low-pressure mode (~60 Pa) at 15 kV acceleration voltage and 1.7 nA probe current with a backscattered electron detector (BSD). The TEM samples were analyzed using a JEOL 2100F TEM (JEOL USA, Peabody, MA) operating at a beam voltage of 200 kV. Bright Field (BF) and High Angle Annular Dark Field (HAADF) images were simultaneously acquired in the STEM mode with a 0.5–1 nm probe size. Elemental analysis was performed at the regions of interest (ROI) with an EDS detector (X-Max80T, Oxford Instruments America, Concord, MA). EELS spectra and energy-filtered TEM (EFTEM) images were obtained using a post-column Gatan Image Filter (GIF) (Tridiem 863, Gatan, Pleasanton, CA). The images and spectra were collected and analyzed with the Digital Micrograph software (Gatan, Pleasanton, CA). Unfiltered and zero-loss (ZL) filtered images were collected to estimate sample thickness variation. Energy-filtered images were acquired in the vicinity of the C-K (284 eV), Cu-$L_{2,3}$ (931 eV), and O-K (532 eV) edges using a 25 eV width slit by applying the three-window method. Alignment was applied to correct specimen drift during the acquisition of the pre-edge and post-edge images. After applying a power-law background model, the elemental distributions of C, Cu, and O were obtained from the filtered images. Core-loss energy-loss spectra were recorded at 200 kV using an energy dispersion of 0.1 eV per

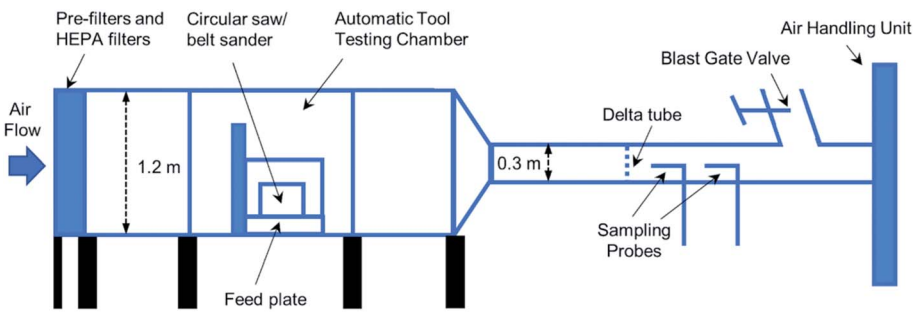

Fig. 1 Diagram of an automatic laboratory tool-testing system for aerosol generation and sampling.

© 2022 The Author(s). Published by the Royal Society of Chemistry

Open Access Article. Published on 11 April 2022. Downloaded on 1/12/2026 6:28:32 AM.
This article is licensed under a Creative Commons Attribution-NonCommercial 3.0 Unported Licence.

channel in the STEM mode with the spot size of 1 nm. Zero-loss and low-loss spectra were acquired and later used to calculate the relative thickness of the sample and remove plural scattering by Fourier-ratio deconvolution. A total of 284 wood dust structures were imaged and analyzed by EELS to determine the Cu species in released airborne particles.

Results and discussion

Particle distribution in MC treated wood

During the pressure treatment process, the liquid flow of preservatives containing insoluble BCC particles enters the wood fibers, travels along the longitudinal pathways, and reaches the radially distributed wood cells after passing the valve-like pits. In this process, most micronized BCC particles are too large to penetrate deep into the wood's microstructure, leaving heavy deposition of copper particles on the surface of the cell wall and interfiber structures.

The micro-distribution of copper particles in the transverse section (TS), radial-longitudinal section (RLS), and tangential-longitudinal section (TLS) of thin section MCA samples are revealed by the SEM backscattered electron (BSE) images in Fig. 2a–c. The copper particles (verified by the EDS analysis in Fig. 2d) were found to accumulate mainly at the inner surfaces of the longitudinal tracheids (Fig. 2a) but not within the cell walls. In the RLS view shown in Fig. 2b, rectangular shapes of copper micro-clusters were observed in the interfiber pits within the ray parenchyma structures. The deposition of copper particles was also seen in the bordered pits (Fig. 2c) distributed within the longitudinal tracheids due to the presence of pit membranes which act as valves to control liquid flows between fibers. The copper residues were not detected in untreated yellow pine samples. The findings of copper distribution in MCA samples are in good agreement with the previous study on the micro-distribution of copper carbonate nanoparticles conducted by Matsunaga *et al.*[6] It should be noted that the distribution and penetration depth of insoluble copper species can vary significantly by the age and type of wood, treatment process, and particular wood structures.[28,29] Moreover, fixation reactions of ionic copper species within the wood cell structures may occur at different stages during the pressure treatment, which further complicates copper detection and quantification.[29] Thus, a considerable variation of the relative abundance of copper species in released particles may exist due to the changes of the actual copper content in the preservative formulas, treatment processes, and structural inhomogeneity of the wood, making copper speciation and quantification difficult.

Copper particles in airborne wood dust

As copper-base preservatives interact with the wood structures during the pressure treatment, they can chemically bond to the reactive sites or deposit onto the impermeable cell pit membranes or walls. As a result, the copper-treated wood can retain a high level of copper in the wood cell components after chemical fixation and drying processes. However, the type and

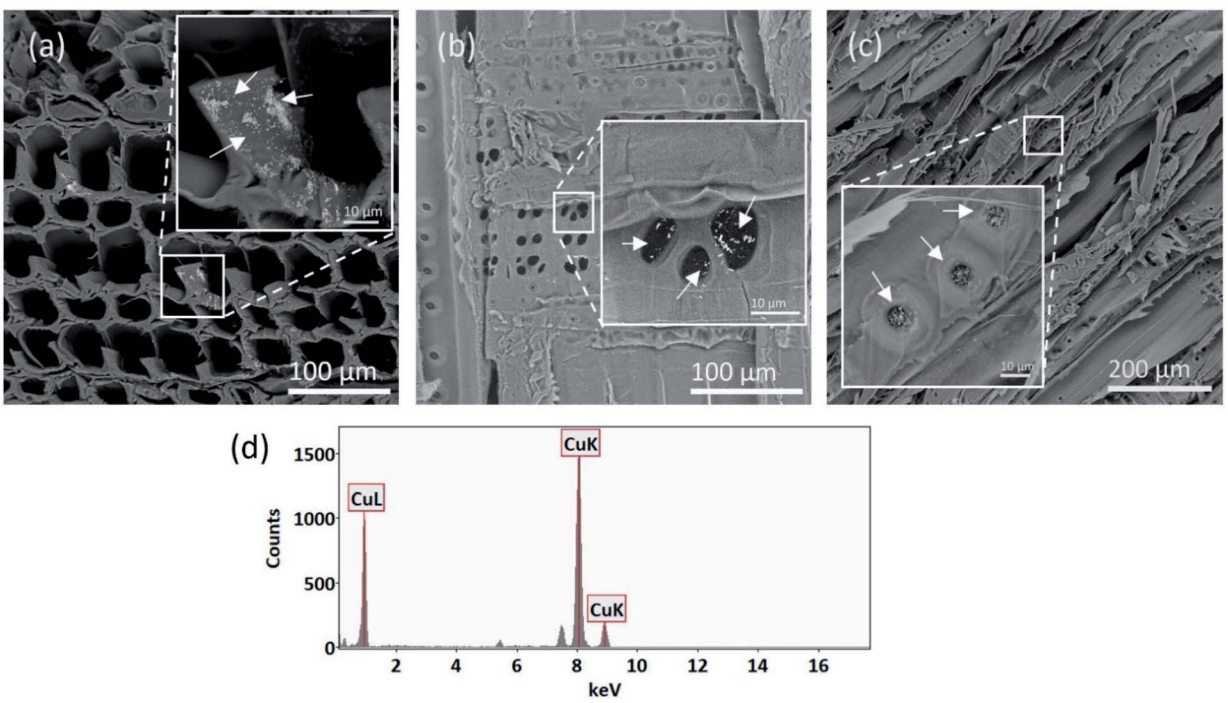

Fig. 2 SEM-BSE images of MC treated wood showing micronized copper particles (bright spots) in (a) transverse (b) radial-longitudinal and (c) tangential sections. The insert images show the specific regions of interest with agglomerated particles pointed by arrows: (a) cell wall, (b) interfiber pits in the ray parenchyma, and (c) cellulose membranes inside the bordered pits of longitudinal tracheids. In addition, EDS analysis (d) was performed to verify the presence of Cu particles.

© 2022 The Author(s). Published by the Royal Society of Chemistry

Open Access Article. Published on 11 April 2022. Downloaded on 1/12/2026 6:28:32 AM.
This article is licensed under a Creative Commons Attribution-NonCommercial 3.0 Unported Licence.

distribution of copper species in wood cells are dominated by several factors such as particle sizes, transport pathways, and the availabilities of deposition/reaction sites where particles accumulate. For insoluble BCC particles, their primary deposition sites were found near the outer surfaces of the cell wall and interfiber pit membranes where limited fluid transport occurs. In contrast, the soluble Cu(II) species can infiltrate cell walls and form a stabilized Cu–wood complex after chemical fixation. Therefore, the availability of the reactive chemical groups (*e.g.*, carboxylate, aromatic esters, and phenolic hydroxyl attached to hemicelluloses and lignins) determines the degree of complexation and particle distribution. It was demonstrated that soluble Cu(II) species tend to bond strongly with carboxylate in hemicellulose by complexation.[10] Wood components with rich hemicellulose content, such as compound middle lamella (CML), are expected to attract and bond more soluble Cu(II) species than cellulose abundant secondary layers (S1, S2, and S3).[30]

During mechanical abrasion or cutting, different forms of airborne dust that contains copper content can be released. By analyzing 284 STEM images of copper-containing structures ranging from 20 nm to 5 μm, five representative dust particle types were identified, as seen in Fig. 3. Most of the images captured by STEM (about 64%) show structures in forms similar to those revealed in Fig. 3a–c, where copper particles (verified by the EDS elemental identification) are embedded in the wood matrices. Specifically, Fig. 3a represents one particular type that contains highly dispersed ultrafine Cu-containing particles that are expected to be Cu complexes chemically bonded to the wood matrices. On the other hand, BCC-like particles were observed in wood dust, showing structures similar to Fig. 3b and c. Similar shapes and aspect ratios were found from these BCC-like particles and those identified in the SEM images. In addition, two types of standalone Cu-containing particles (each accounted for about 18% of total structures counted, as seen in Fig. 3d and e) were identified: one exhibits BCC-like rectangular shape, and another shows spherical core–shell structure. It was demonstrated that nanoparticles smaller than the typical threshold sizes of nanopores of cell walls could enter the percolation pathways of wood components *via* pores in the pit membranes.[31,32] This may explain the finding of isolated spherical Cu-containing particles (as seen in Fig. 3e). The variation of shapes, sizes, and distributions of particles within the investigated systems indicate that further copper speciation is needed. The chemistry of copper content and wood matrices was then analyzed using EELS. The detailed analysis is discussed in the following section.

EELS analysis of Cu compounds

When energetic electrons interact with an atom, the core–shell electrons can be excited to the unoccupied higher energy levels. The active transitions associated with this process can be characterized by the core-loss EELS. In core-loss EELS and X-ray absorption spectra (XAS) for 3d transition metals, there are two narrow and intense peaks, called "white lines" (WLs), at the onsets of the L_2 and L_3 absorption edges.[33] These WLs (*i.e.*, L_2 and L_3) are associated with the transitions of $2p_{1/2}$ and $2p_{3/2}$

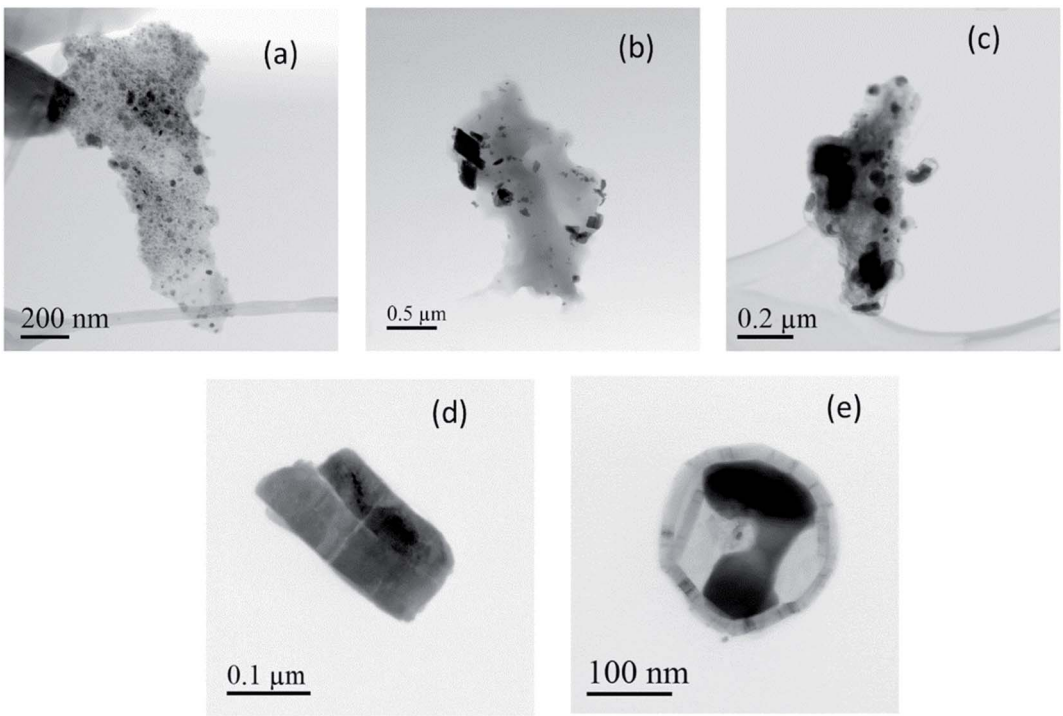

Fig. 3 STEM-BF images showing different shapes and sizes of copper-containing particles (dark contrast) in the aerosol samples collected during sawing or sanding of MC-treated wood. Micro- and/or nano-sized particles are embedded in the wood matrices (a–c) or standalone as free particles (d–e).

Open Access Article. Published on 11 April 2022. Downloaded on 1/12/2026 6:28:32 AM.
This article is licensed under a Creative Commons Attribution-NonCommercial 3.0 Unported Licence.

electrons to the unoccupied 3d density of states (DOS). Many studies[33–36] have shown that the relative intensities, widths, and threshold energies of these WLs can be used for characterizing the oxidation states of the 3d transition metals and their compounds. With the improved energy resolution in EELS, details about the local chemical bonding information can be revealed from the energy loss near edge structures (ELNES) with similar features as in the X-ray absorption near edge structure (XANES). To investigate the presence of different Cu species in the released wood dust (WD) particles, core-loss EEL spectra were acquired from individual Cu reference materials (Cu, Cu_2O, CuO, $CuCO_3 \cdot Cu(OH)_2$, and $Cu(OAc)_2$) as analogs for Cu compounds that might be present in the collected samples.

Fig. 4a shows background subtracted and deconvoluted Cu-$L_{2,3}$ edge spectra of reference Cu materials acquired in the identical experimental conditions. In addition to the $L_{2,3}$ edges, minor peaks (a–f) near the L_3 edges were visible for Cu, Cu_2O, and $CuCO_3 \cdot Cu(OH)_2$ reference materials. The $L_{2,3}$ energies and their full width at half maximum (FWHM), the relative energy intensity, and near-edge peak locations are reported in Table 1 for each reference material. As seen in Fig. 4a, all reference materials except for Cu and $Cu(OAc)_2$ show prominent white lines at the onset of L_3 and L_2 edges due to the transition of $2p_{3/2}$ and $2p_{1/2}$ electrons to the highest unoccupied 3*d* states. Because of the entirely occupied 3*d* band, no white lines were present in the spectrum of Cu. Additionally, two bumps (denoted as peaks a and b) were observed at about 4 eV and 8 eV above the L_3 threshold energy, agreeing with the previous EELS and XAS measurements.[33,37,38] Other near-edge peaks (denoted as peaks c–f) possibly due to 4s transitions were observed for and $CuCO_3 \cdot Cu(OH)_2$. Noticeable energy shifts (*i.e.*, chemical shifts) of L_3 peaks were detected in spectra for Cu_2O (+0.3 eV), CuO (−2.2 eV), and $CuCO_3 \cdot Cu(OH)_2$ (−1 eV) when compared to the L_3 step of Cu located at 933.8 eV. In comparison to the sharp and narrow L_3 peaks of Cu(I) and Cu(II) oxides, L_3 peaks in basic copper carbonate and Cu(II) acetate were both broadened. It has been demonstrated that the changes of chemical shift and peak width may indicate the transition of coordination states of Cu(II) species.[39] Besides peak onset energies and widths, the white line intensity ratio was also evaluated. Theoretically, this ratio is expected to be 2 : 1 for 3d transition metals due to the statistical ratio of the initial states.[33] In practice, this ratio can shift significantly depending on the elements and corresponding d-band occupancy.[33,35] Among all reference materials summarized in Table 1, Cu(I) oxides exhibit the highest L_3–L_2 ratio (>2 : 1). Because of the attenuated $L_{2,3}$ edges, this ratio was significantly reduced to 0.8 and 0.7 for Cu and Cu(II) acetate, respectively. It is noted that the measured $L_{2,3}$ features can be affected by the hardware of the EELS system and how EELS data was processed. Therefore, EELS data of aerosol samples were acquired using the same experimental setup and analyzed using the same approach to extract the Cu-$L_{2,3}$ features.

The two-parameter plot in Fig. 4b shows the correlation of measured $L_{2,3}$ features for different Cu compounds in samples

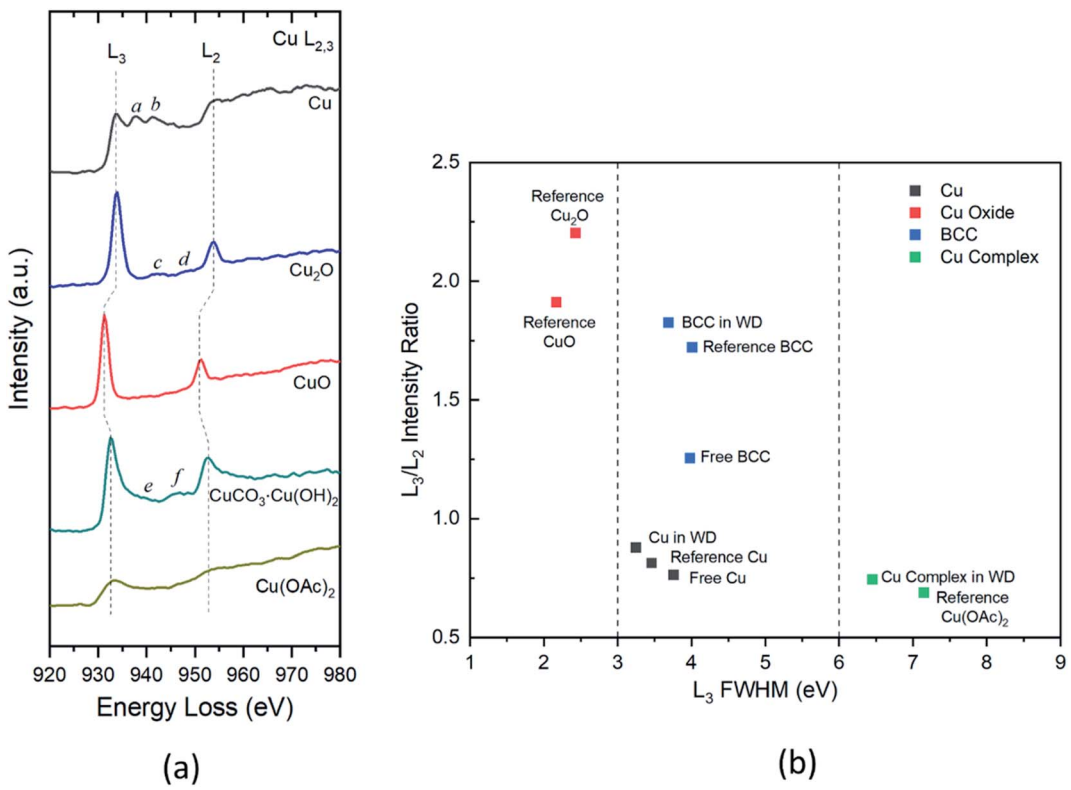

Fig. 4 (a) Background subtracted and deconvoluted Cu-$L_{2,3}$ spectra of reference Cu materials showing the L_3 and L_2 features and near-edge structures; (b) L_3 FWHM *vs.* L_3/L_2 intensity ratio plot of Cu compounds present in the air samples and reference materials. The symbol's color indicates different Cu species: black: Cu; red: Cu(I) and Cu(II) oxides; blue: BCC; green: Cu organic complex.

© 2022 The Author(s). Published by the Royal Society of Chemistry

Open Access Article. Published on 11 April 2022. Downloaded on 1/12/2026 6:28:32 AM.
This article is licensed under a Creative Commons Attribution-NonCommercial 3.0 Unported Licence.

Table 1 Cu-$L_{2,3}$ edge energies and corresponding full width at half maximum (FWHM), L_3/L_2 intensity ratio, and near-edge peak energies of Cu reference materials (measured from spectra with 0.1 eV per channel)

Reference materials	L_3 (FWHM) (eV)	L_2 (FWHM) (eV)	L_3/L_2 intensity ratio[a]	Near-edge peaks (eV)
Cu[b]	933.8 (3.5)	953.6 (10.1)	0.8	(a) 937.6; (b) 941.4
Cu_2O	934.1 (2.4)	953.8 (4.2)	2.2	(c) 942.8; (d) 948.2
CuO	931.6 (2.2)	951.2 (3.7)	1.9	
$CuCO_3 \cdot Cu(OH)_2$	932.8 (4.0)	952.8 (6.1)	1.7	(e) 939.4; (f) 946.6
$Cu(OAc)_2$	933.2 (7.2)	953.4 (16.1)	0.7	

[a] Determined by fitted areas of L_3 and L_2 peaks. [b] Measurements for Cu refer to the L_3 and L_2 steps.

and reference materials. In this plot, the Cu species can be differentiated by their L_3 FWHM and relative intensity of L_3 and L_2. For Cu(I) and Cu(II) oxides, they can be well characterized by the sharp and narrow L_3 peaks with FWHM < 3 eV and L_3/L_2 intensity ratio at about 2. In contrast, the Cu–wood complex and reference Cu(II) acetate both present similar shapes of L_3 and L_2 with widths about 7 eV and an intensity ratio of about 1. As depicted in Fig. 4b, the L_3 FWHM of BCC and Cu are falling in the range from 3 to 6 eV. BCC and Cu can be differentiated on the plot by their vastly different L_3/L_2 ratios. The BCC embedded in the wood dust presents a similar L_3/L_2 ratio as the reference BCC. In contrast, the free BCC shows a somewhat reduced L_3/L_2 ratio indicating the potential changes of chemical states. A smaller L_3/L_2 ratio (~0.8) was observed for Cu, clearly distinguishable from the ratio of BCC and Cu oxides. These findings of characteristic Cu-$L_{2,3}$ edges can be used to identify different Cu species effectively.

Structural and chemical determination of Cu particles

Energy-filtered TEM (EFTEM) and EELS were performed to investigate the distribution of copper species and their specific chemical states in the released dust particles. The EFTEM and STEM-BF images (Fig. 5a–f) show the distributions of Cu in the wood matrices of two representative wood dust types: small aggregates (5–30 nm) are homogeneously distributed within the matrix of one type shown in Fig. 5a, c and e, whereas rectangular shape particles (~100–200 nm) are seen in a slightly condense matrix in Fig. 5b, d and f. EELS spectra (Fig. 5g) show the Cu-$L_{2,3}$ edges of three typical copper aggregates within the matrices (Fig. 5e and f) and those of the reference materials measured under the same experimental conditions. By examining the positions, shapes, and relative intensity of Cu-$L_{2,3}$ signature peaks, three Cu-containing structures were identified as (I) Cu–wood complex, (II) Cu, and (III) BCC.

Two types of free Cu-containing particles shown in Fig. 6 were analyzed by EFTEM and EELS to determine their chemical composition and oxidation states. As revealed by the SEM images, insoluble BCC particles are more likely to agglomerate on the surfaces of cell walls and interfiber pits. During sanding/sawing processes, some BCC particles may be dislodged from their deposition sites and released into the air as standalone particles. EELS analysis confirms that the individual particle in Fig. 6c has almost identical elemental composition and Cu-$L_{2,3}$ edge features as reference BCC. It also determines that the core of spherical particle in Fig. 6d mainly consists of Cu, exhibiting similar Cu-$L_{2,3}$ edges as those embedded in the large wood matrices (such as particle III in Fig. 5e).

As revealed by the STEM images and EELS analysis, the formation and distribution of these Cu species in copper-treated wood are expected to be affected by the wood chemistry. It is known that wood is a heterogeneous natural nanocomposite comprising of three primary chemical ingredients (by mass): cellulose (40–50%), hemicellulose (25–35%), and lignin (18–35%).[30] The availability of reactive chemical groups (*e.g.*, carboxylate, aromatic esters, and phenolic hydroxyl) attached to the hemicelluloses and lignin components determine the wood acid/base properties and reactivities.[30] In particular, Cu(II) ions are more likely to react with the carboxylic acid groups in the hemicellulose-rich components,[10] forming Cu–wood complexed structures similar to region (I) in Fig. 5e. In contrast, the distribution of BCC particles is associated with the cellulose and lignin concentrations in the wood components.[40] The reduced Cu form (*i.e.*, Cu) was found in the wood matrices (Fig. 5e) and standalone particles (Fig. 6d). This finding agrees with the previous studies[10,29] showing a small amount (<5%) of reduced copper species in copper-treated wood. Considering the complexity of Cu–wood interactions, these reduced Cu forms may originate from the ingredients to formulate the copper preservatives or chemical transformation in pressure treatment and environmental exposure after production.

In addition to the three primary chemical ingredients, a small number of inorganic minerals and organic extractives also contribute 4–10% of the total mass in wood.[30] Among them, calcium is considered an essential element in forming wood cell walls, particularly in cross-linking carboxyl groups within the pectin layer and lignification.[5,30,41] Therefore, the calcium concentration is regarded as an important indicator for lignin content level.[42,43]

STEM-BF images and core-loss EELS in a range covering the C-K, Ca-$L_{2,3}$, and O-K edges were acquired to investigate the chemistry of two types of wood matrices (Fig. 7). The images show different matrix textures and morphologies of embedded copper particles. One type shown in Fig. 7a contains elongated BCC particles embedded in a plain matrix. In contrast, the second type of wood dust in Fig. 7c shows a fibrous matrix occupied by the small precipitates composed of the Cu–wood complexes. A small Cu-free region in the wood matrix of each structure (see Fig. 7b and d) was selected for EELS analysis to determine the chemical composition of the matrix. As shown in

Open Access Article. Published on 11 April 2022. Downloaded on 1/12/2026 6:28:32 AM.
This article is licensed under a Creative Commons Attribution-NonCommercial 3.0 Unported Licence.

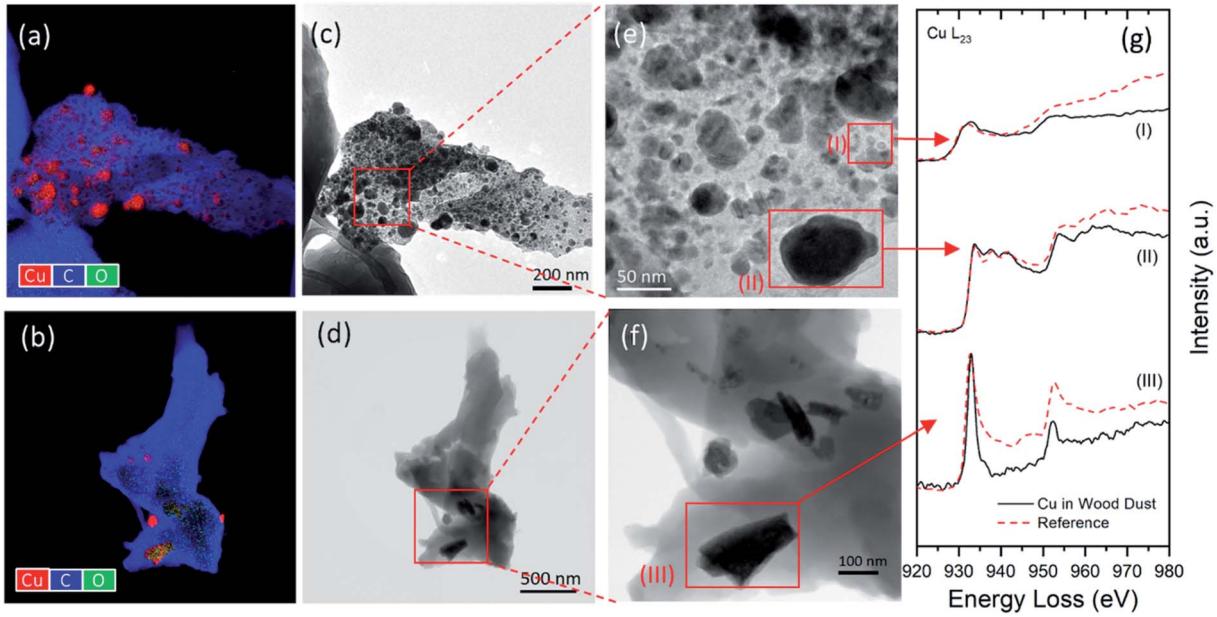

Fig. 5 (a and b) EFTEM maps showing the elemental distributions of Cu, C, and O in the wood matrices; (c and d) STEM-BF images of the wood dust particles with chosen regions containing different copper species; (e and f) selected aggregated particles for EELS analysis; (g) corresponding EELS Cu $L_{2,3}$ edges and comparisons with the spectra of reference materials: (I) $Cu(OAc)_2$, (II) Cu, (III) $CuCO_3 \cdot Cu(OH)_2$.

Fig. 7e, almost identical π^* and σ^* peak features of the C-K edge indicate that the two materials have similar carbon bonding chemistry. Oxygen element was detected in both materials, as evidenced by the appearance of O-K peaks. The Ca-$L_{2,3}$ peaks were only seen in the first structure. The calcium detected in such matrix suggests that this wood dust type may derive from the highly lignified cell wall regions such as the S3 layer, cell corner (CC), and compound middle lamella (CML).[44,45] Previous

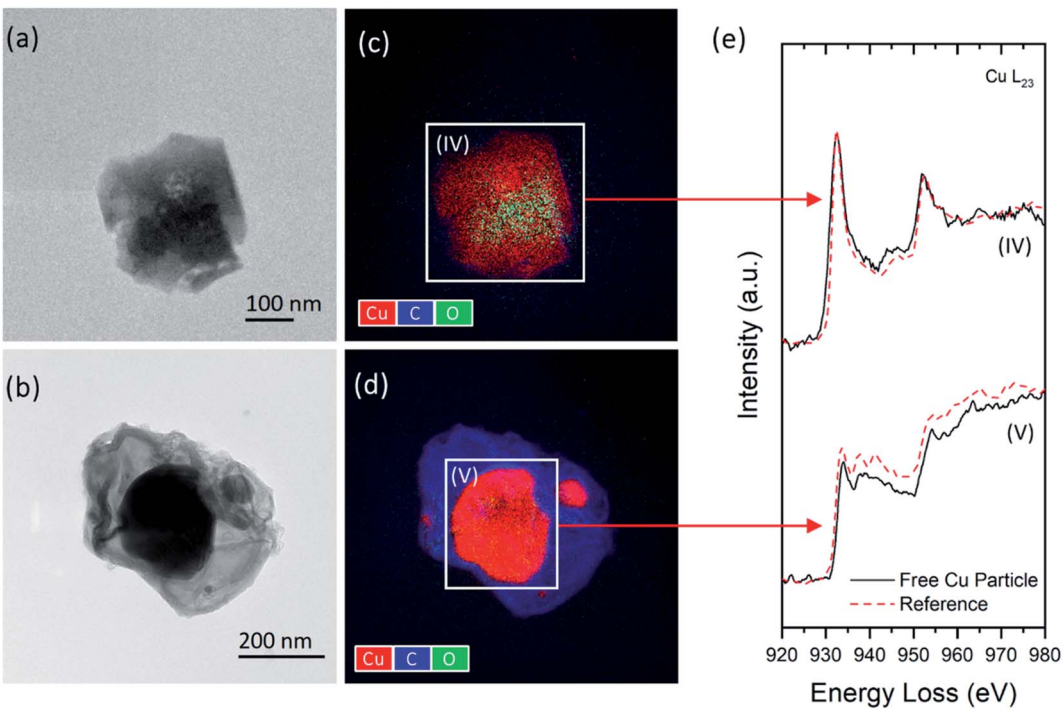

Fig. 6 (a and b) STEM-BF images of two types of standalone copper particles; (c and d) corresponding EFTEM maps showing the elemental distributions and regions of interest for EELS analysis; (e) EELS Cu $L_{2,3}$ edges of selected particles and reference spectra of (IV) $CuCO_3 \cdot Cu(OH)_2$ and (V) Cu.

© 2022 The Author(s). Published by the Royal Society of Chemistry

Open Access Article. Published on 11 April 2022. Downloaded on 1/12/2026 6:28:32 AM.
This article is licensed under a Creative Commons Attribution-NonCommercial 3.0 Unported Licence.

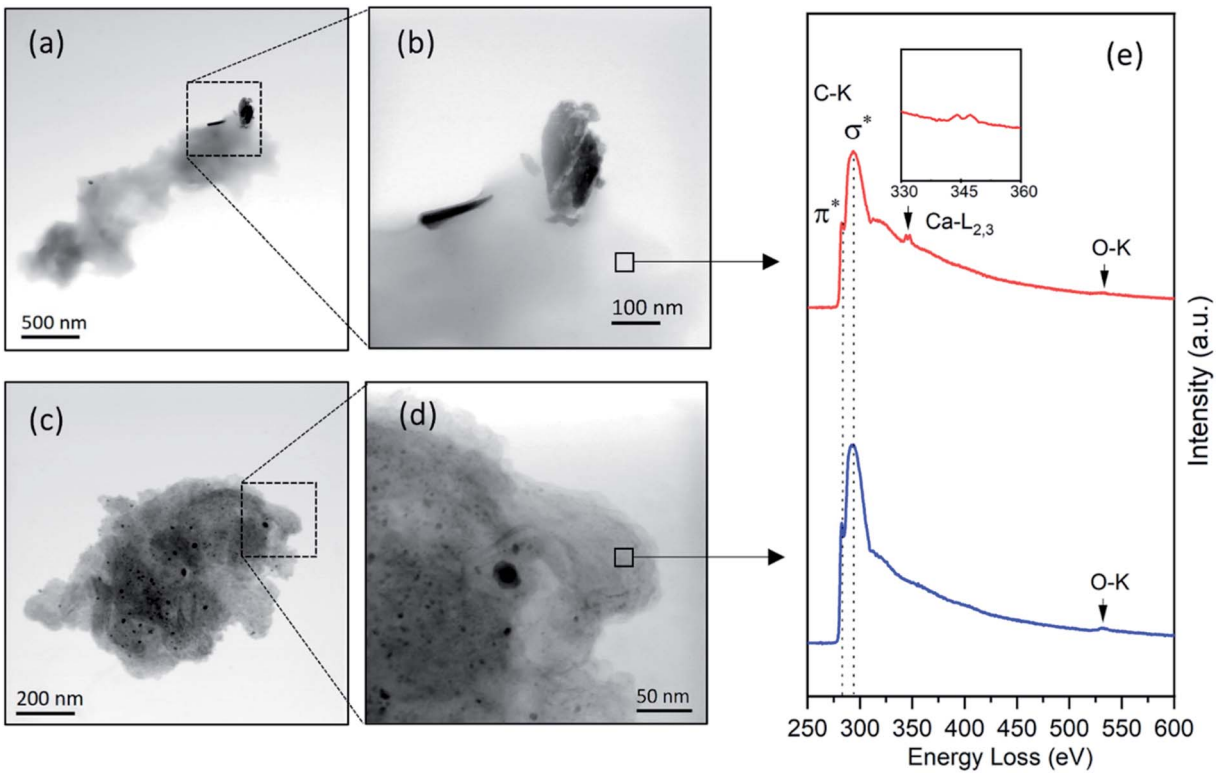

Fig. 7 STEM-BF images of (a and b) lignified wood dust with BCC particles attached to the edges; (c and d) fibrous wood dust with embedded ultrafine particles; (e) EELS spectra of selected areas in a range covering C-K, Ca-$L_{2,3}$, and O-K edges, showing different chemical compositions of the two types of wood matrices. The inset of (e) shows the signature Ca-$L_{2,3}$ peaks.

studies of the correlation between the copper carbonate distributions and the lignin concentrations suggest that more BCC particles are likely found in the lignified structures.[40] Therefore, the structures similar to Fig. 7a were classified as a highly lignified matrix with embedded BCC particles. In contrast to insoluble copper carbonate, the Cu(II) ions mainly interact with the wood components through complexation reactions with the carboxyl groups of hemicelluloses and pectins.[46,47] A wood component with a high concentration of hemicelluloses would become especially attractive to mobile Cu(II) ions to form Cu–wood complexes. Unlike a lignin-rich matrix, the microfibrillar matrix (Fig. 7c) likely formed by hemicelluloses can provide more reactive sites for Cu(II) ions in the complexation. These sites are often spread over the entire hemicellulose-rich structure, leading to a more homogeneous distribution of ionic Cu(II) species than other insoluble Cu species.

Conclusion

In this study, we presented a new approach for sampling and characterizing nanoscale Cu particles in airborne wood dust. Micro-distribution of insoluble copper particulates in copper-treated wood was investigated by SEM to understand their formation and localization in specific wood components. The presence of copper precipitates was confirmed in various locations from multi-directional views of SEM images. The accumulation of copper particles was primarily observed on the surface of the cell wall and within the openings that connect the cellular elements of the wood. STEM imaging and EELS analysis were employed to investigate the microstructures and chemical properties of micro-/nanoscale Cu particles released during sanding/sawing MC-treated lumber in a laboratory testing chamber. We have demonstrated using EELS Cu $L_{2,3}$ edges with reference spectra to determine the Cu species, oxidation state, and coordination environment for Cu-containing nanoparticles. Three types of species, including basic copper carbonate (BCC), Cu, and Cu–wood complex, were identified. Although most copper species were found embedded in wood dust, the unbound copper particles also exist as a form of BCC or reduced Cu. The micro-distribution of copper-containing particles within wood matrices can be affected by the distribution and chemistry of specific wood components, which is evidenced by the STEM images and EELS analysis. Our studies show that the distribution of BCC particles is associated with the lignification level of the specific wood components, and Cu complexes are more likely distributed in structures that contain a high level of hemicelluloses. Once released into the environment, three types of Cu species and their different affinity to the wood matrices may affect the fate and chemical transformation during their life cycles. It is noted that a considerable variation of the relative abundance of copper species in released particles may exist due to the inhomogeneous nature of the wood structures. The actual copper species and their distribution in copper-treated lumber may vary among the different brands,

Open Access Article. Published on 11 April 2022. Downloaded on 1/12/2026 6:28:32 AM. This article is licensed under a Creative Commons Attribution-NonCommercial 3.0 Unported Licence.

preservative formulations, and production methods. Therefore, precise measurement and quantification of copper content remain challenging. However, the findings of this study provide baseline information on characteristics of released Cu NPs during sanding/sawing copper-treated wood. The sampling and analytical microscopy techniques proposed in this study also pave the way for developing new methods for characterizing complex engineering nanomaterials that pose potential environmental and occupational hazards.

Disclaimer

The findings and conclusions in this report are those of the authors and do not necessarily represent the official position of the National Institute for Occupational Safety and Health, Centers for Disease Control and Prevention.

Conflicts of interest

There are no conflicts to declare.

Acknowledgements

We gratefully acknowledge funding for this work through the Nanotechnology Research Center (NTRC) of the National Institute for Occupational Safety and Health (NIOSH) (NTRC-93908M5).

References

1 M. H. Freeman and C. R. McIntyre, A Comprehensive Review of Copper-Based Wood Preservatives, *For. Prod. J.*, 2008, **58**, 6–27.
2 T. P. Schultz, H. Militz, M. H. Freeman, B. Goodell and D. D. Nicholas, Development of Commercial Wood Preservatives, *ACS Symposium Series 982: Development of Commercial Wood Preservatives*, 2008, p. 982, DOI: **10.1021/bk-2008-0982**.
3 P. Evans, H. Matsunaga and M. Kiguchi, Large-scale application of nanotechnology for wood protection, *Nat. Nanotechnol.*, 2008, **3**, 577.
4 S. Schmitt, J. Zhang, S. Shields and T. Schultz, in *Deterioration and Protection of Sustainable Biomaterials*, ed. T. P. Schultz, B. Goodell and D. D. Nicholas, American Chemical Society, Washington, DC, 2014, pp. 217–225.
5 N. Schiopu and L. Tiruta-Barna, in *Toxicity of building materials*, ed. F. P. Torgal, S. Jalali and A. Fucic, Woodhead, Cambridge, 2012, pp. 138–165.
6 H. Matsunaga, M. Kiguchi and P. D. Evans, Microdistribution of copper-carbonate and iron oxide nanoparticles in treated wood, *J. Nanopart. Res.*, 2009, **11**, 1087–1098.
7 H. L. Karlsson, J. Gustafsson, P. Cronholm and L. Möller, Size-dependent toxicity of metal oxide particles–a comparison between nano- and micrometer size, *Toxicol. Lett.*, 2009, **188**, 112–118.
8 K. Midander, P. Cronholm, H. L. Karlsson, K. Elihn, L. Möller, C. Leygraf and I. O. Wallinder, Surface characteristics, copper release, and toxicity of nano- and micrometer-sized copper and copper(II) oxide particles, *Small*, 2009, **5**, 389–399.
9 M. Ahamed, M. J. Akhtar, H. A. Alhadlaq and S. A. Alrokayan, Assessment of the lung toxicity of copper oxide nanoparticles, *Nanomedicine*, 2015, **10**, 2365–2377.
10 W. Xue, J. N. R. Ruddick and P. Kennepohl, Solubilisation and chemical fixation of copper(II) in micronized copper treated wood, *Dalton Trans.*, 2016, **45**, 3679–3686.
11 Z. Wang, A. von dem Bussche, P. K. Kabadi, A. B. Kane and R. H. Hurt, Biological and environmental transformations of copper-based nanomaterials, *ACS Nano*, 2013, **7**, 8715–8727.
12 W. Xue, P. Kennepohl and J. N. R. Ruddick, Reacted copper(II) concentrations in amine amended micronized copper treated red pine and lodgepole pine, *Eur. J. Wood Wood Prod.*, 2018, **76**, 337–343.
13 W. Xue, P. Kennepohl and J. N. Ruddick, Investigation of copper solubilization and reaction in micronized copper treated wood by electron paramagnetic resonance (EPR) spectroscopy, *Holzforschung*, 2012, **66**(7), 889–895.
14 S. L. Zelinka, J. E. Jakes, G. T. Kirker, L. Passarini, C. G. Hunt, B. Lai, O. Antipova, L. Li and S. Vogt, Copper distribution and oxidation states near corroded fasteners in treated wood, *SN Appl. Sci.*, 2019, **1**, 6.
15 C. Civardi, J. van den Bulcke, M. Schubert, E. Michel, M. I. Butron, M. N. Boone, M. Dierick, J. van Acker, P. Wick and F. W. M. R. Schwarze, Penetration and Effectiveness of Micronized Copper in Refractory Wood Species, *PLoS One*, 2016, **11**, e0163124.
16 W. E. Platten, N. Sylvest, C. Warren, M. Arambewela, S. Harmon, K. Bradham, K. Rogers, T. Thomas and T. P. Luxton, Estimating dermal transfer of copper particles from the surfaces of pressure-treated lumber and implications for exposure, *Sci. Total Environ.*, 2016, **548–549**, 441–449.
17 V. Marchetti, J. Ghanbaja, P. Gérardin and B. Loubinoux, Localisation and Characterization by TEM and EELS of Man-ganese Species during Graft Copolymerization of Acrylic Acid onto Sawdust Using KMnO4 as Initiator, *Holzforschung*, 2000, **54**, 2102.
18 M. Reza, E. Kontturi, A. S. Jääskeläinen, T. Vuorinen and J. Ruokolainen, Transmission Electron Microscopy for Wood and Fiber Analysis – A Review, *BioResources*, 2015, **10**(3), 6230–6261.
19 N. Browning, D. Wallis, P. Nellist and S. Pennycook, EELS in the STEM: Determination of materials properties on the atomic scale, *Micron*, 1997, **28**, 333–348.
20 J. D. Sisler, C. Qi, W. McKinney, J. Shaffer, M. Andrew, T. Lee, T. Thomas, V. Castranova, R. R. Mercer and Y. Qian, Physical chemical properties and cell toxicity of sanding copper-treated lumber, *J. Occup. Environ. Hyg.*, 2018, **15**, 311–321.
21 C. Qi, A. Echt and M. G. Gressel, On the Characterization of the Generation Rate and Size-Dependent Crystalline Silica

© 2022 The Author(s). Published by the Royal Society of Chemistry

Open Access Article. Published on 11 April 2022. Downloaded on 1/12/2026 6:28:32 AM. This article is licensed under a Creative Commons Attribution-NonCommercial 3.0 Unported Licence.

Content of the Dust from Cutting Fiber Cement Siding, *Ann. Occup. Hyg.*, 2016, **60**, 220–230.

22 C. Wang, C. Qi, A. K. Dozier, J. E. Fernback and P. Kulkarni, Microstructure and Chemical Characterization of Copper Nanoparticles in Wood Dust by TEM/STEM, *Microsc. Microanal.*, 2018, **24**, 1762–1763.

23 NIOSH, *Method 7402 Asbestos by TEM in NIOSH Manual of Analytical Methods*, U.S. Department of Health and Human Services, Centers for Disease Control and Prevention, National Institute for Occupational Safety and Health, DHHS (NIOSH), Cincinnati, OH, 4th edn, 1994.

24 NIOSH, *NIOSH Manual of Analytical Methods. Publication No. 2014-151*, U.S. Department of Health and Human Services, Centers for Disease Control and Prevention, National Institute for Occupational Safety and Health, DHHS (NIOSH), Cincinnati, OH, 5th edn, 2017.

25 J. E. Brockmann, in *Aerosol measurement*, ed. P. A. Baron, P. Kulkarni and K. Willeke, Wiley, Hoboken, N.J., 3rd edn, 2011, pp. 68–105.

26 M. E. Birch, C. Wang, J. E. Fernback, H. A. Feng, Q. T. Birch and A. K. Dozier, in *NIOSH Manual of Analytical Methods*, U.S. Department of Health and Human Services, Centers for Disease Control and Prevention, National Institute for Occupational Safety and Health, DHHS (NIOSH), Cincinnati, OH, 5th edn, 2017.

27 M. M. Dahm, M. K. Schubauer-Berigan, D. E. Evans, M. E. Birch, J. E. Fernback and J. A. Deddens, Carbon Nanotube and Nanofiber Exposure Assessments: An Analysis of 14 Site Visits, *Ann. Occup. Hyg.*, 2015, **59**, 705–723.

28 C. Civardi, L. Schlagenhauf, J.-P. Kaiser, C. Hirsch, C. Mucchino, A. Wichser, P. Wick and F. W. M. R. Schwarze, Release of copper-amended particles from micronized copper-pressure-treated wood during mechanical abrasion, *J. Nanobiotechnol.*, 2016, **14**, 77.

29 S. L. Zelinka, G. T. Kirker, J. E. Jakes and L. Passarini, Distribution and Oxidation State of Copper in the Cell Walls of Treated Wood Examined by Synchrotron Based XANES and XFM, *American Wood Protection Association*, 2017, pp. 172–178.

30 R. Pettersen, *The Chemical Composition of Wood. The Chemistry of solid wood*, American Chemical Society, Washington, D.C., 1984.

31 B. Choat, M. Ball, J. Luly and J. Holtum, Pit membrane porosity and water stress-induced cavitation in four co-existing dry rainforest tree species, *Plant Physiol.*, 2003, **131**, 41–48.

32 L. Pereira, D. N. A. Flores-Borges, P. R. L. Bittencourt, J. L. S. Mayer, E. Kiyota, P. Araújo, S. Jansen, R. O. Freitas, R. S. Oliveira and P. Mazzafera, Infrared Nanospectroscopy Reveals the Chemical Nature of Pit Membranes in Water-Conducting Cells of the Plant Xylem, *Plant Physiol.*, 2018, **177**, 1629–1638.

33 R. D. Leapman, L. A. Grunes and P. L. Fejes, Study of the L23 edges in the 3d transition metals and their oxides by electron-energy-loss spectroscopy with comparisons to theory, *Phys. Rev. B: Condens. Matter Mater. Phys.*, 1982, **26**, 614–635.

34 H. Tan, J. Verbeeck, A. Abakumov and G. van Tendeloo, Oxidation state and chemical shift investigation in transition metal oxides by EELS, *Ultramicroscopy*, 2012, **116**, 24–33.

35 D. H. Pearson, C. C. Ahn and B. Fultz, White lines and d-electron occupancies for the 3d and 4d transition metals, *Phys. Rev. B: Condens. Matter Mater. Phys.*, 1993, **47**, 8471–8478.

36 G. Akgül, F. Aksoy, A. Bozduman, O. M. Ozkendir, Y. Ufuktepe and J. Lüning, Study of the L2,3 edges of 3d transition metals by X-ray absorption spectroscopy, *Thin Solid Films*, 2008, **517**, 1000–1004.

37 M. Grioni, J. B. Goedkoop, R. Schoorl, F. M. F. de Groot, J. C. Fuggle, F. Schäfers, E. E. Koch, G. Rossi, J.-M. Esteva and R. C. Karnatak, Studies of copper valence states with Cu L3 X-ray-absorption spectroscopy, *Phys. Rev. B: Condens. Matter Mater. Phys.*, 1989, **39**, 1541–1545.

38 M. Grioni, J. F. van Acker, M. T. Czyżyk and J. C. Fuggle, Unoccupied electronic structure and core-hole effects in the x-ray-absorption spectra of Cu_2O, *Phys. Rev. B: Condens. Matter Mater. Phys.*, 1992, **45**, 3309–3318.

39 K. Shimizu, H. Maeshima, H. Yoshida, A. Satsuma and T. Hattori, Ligand field effect on the chemical shift in XANES spectra of Cu(II) compounds, *Phys. Chem. Chem. Phys.*, 2001, **3**, 862–866.

40 L. Santiago-Rodríguez, J. L. Griggs, K. D. Bradham, C. Nelson, T. Luxton, W. E. Platten and K. R. Rogers, Assessment of the bioaccessibility of micronized copper wood in synthetic stomach fluid, *Environ. Nanotechnol., Monit. Manage.*, 2015, **4**, 85–92.

41 A. Berglund, H. Brelid, A. Rindby and P. Engström, Spatial Distribution of Metal Ions in Spruce Wood by Synchrotron Radiation Microbeam X-Ray Fluorescence Analysis, *Holzforschung*, 1999, **53**, 474–480.

42 C. Ravat, F. Monteil-Rivera and J. Dumonceau, Metal Ions Binding to Natural Organic Matter Extracted from Wheat Bran: Application of the Surface Complexation Model, *J. Colloid Interface Sci.*, 2000, **225**, 329–339.

43 X. Guo, S. Zhang and X. Shan, Adsorption of metal ions on lignin, *J. Hazard. Mater.*, 2008, **151**, 134–142.

44 J. Fromm, Wood formation of trees in relation to potassium and calcium nutrition, *Tree Physiol.*, 2010, **30**, 1140–1147.

45 J. Fromm, B. Rockel, S. Lautner, E. Windeisen and G. Wanner, Lignin distribution in wood cell walls determined by TEM and backscattered SEM techniques, *J. Struct. Biol.*, 2003, **143**, 77–84.

46 H. Chen, *Biotechnology of Lignocellulose*, Springer Netherlands, Dordrecht, 2014.

47 E. Sjostrom, The origin of charge on cellulosic fibers, *Nord. Pulp Pap. Res. J.*, 1989, **4**, 90–93.

© 2022 The Author(s). Published by the Royal Society of Chemistry